Residual Stress Generation in Laser-Assisted Cold Spray Deposition of Oxide Dispersion Strengthened Fe$_{91}$Ni$_8$Zr$_1$

Dallin J. Barton[1] · Venkata Satish Bhattiprolu[1] · Billy Chad Hornbuckle[2] ·
Clio M. Batali[1] · Kristopher A. Darling[2] · Gregory B. Thompson[1] ·
Luke N. Brewer[1]

Abstract This paper examines the residual stresses generated by laser-assisted cold spray deposition of an iron-based oxide dispersion strengthened alloy (Fe$_{91}$Ni$_8$Zr$_1$ - at.%) on an AISI 1018 mild steel substrate, as well as studies of the effect of the laser heating on the substrate alone. The in-plane residual stress values were determined by X-ray diffraction-based measurements. In the top section of the layers, established at a raster deposition rate of 25 mm/s and simultaneous surface heating temperatures of 650 and 950 °C, stresses were compressive ranging from − 170 to − 440 MPa. For the substrate only study, a larger span of surface temperatures from 350 to 950 °C and scan rates of 5 and 25 mm/s were investigated. Here, the stresses in the laser tracks were tensile, of the order of + 400 MPa, with both "W''- and "M"- shaped profiles about the laser centerline. It was found that the stress profile shape was influenced by the Gaussian power distribution across the laser spot diameter which correlated with microstructural changes (martensite formation) in the substrate.

Introduction

Cold gas dynamic spray (Ref 1), now commonly shortened to the term cold spray (CS), is a solid-state bonding process that additively deposits metal powders at temperatures much lower than their melting temperatures. This is achieved by spraying the powder at supersonic velocities whereupon its cold weld bonds to either a substrate or to prior deposited material upon contact. This allows CS deposit microstructures (and its resultant properties) to largely be retained, albeit highly deformed. This contrasts with higher temperature coating processes where the material undergoes solidification phase transformation that may degrade the properties. Certain cases of CS additive repair and additive manufacturing are now considered for production (Ref 2, 3).

To date, most of the CS research has been limited to alloys of lower strengths because of the required particle deformation upon impact; however, higher strength alloy deposition is now being research through the development of more favorable CS deposition conditions, which includes increasing the substrate surface temperature to improve deposition adhesion.

Substrate heating can be achieved through the use of a laser which confines the heat zone to the directly deposited region. It also allows for a temporally shorter time at temperature, limiting potential diffusional-based

✉ Luke N. Brewer
lnbrewer1@eng.ua.edu

1   Department of Metallurgical and Materials Engineering, The University of Alabama, Box 870202, Tuscaloosa, AL 35401-0200, USA

2   United States Army Research Laboratory, Weapons and Materials Research Directorate, RDRL-WMM-B, Aberdeen Proving Grounds, MD 21005-5069, USA

transformations and growths in the microstructure as seen in other metal surface laser processing methods (Ref 4). The linking of the in situ laser heating with the CS deposition is referred to as either laser-assisted cold spray (LACS), or supersonic laser deposition, and is emerging as a new means to allow these previously difficult-to-spray materials and/or gas conditions to become more accessible for CS. Materials and conditions that have used this technology include the following: Ti (Ref 5), Stellite (cobalt-chromium alloys, including W-reinforced Stellite) (Ref 6, 7), Al-12Si (Ref 8), Ni-based Inconel 718 (nickel chromium alloy) (Ref 9), diamond/Ni60 composite (Ref 10), TiO_2-Zn (Ref 11), low-pressure cold spray of Cu and Ni with Al_2O_3 additions (Ref 12), and oxide dispersion strengthened (ODS) alloys (Ref 13).

Of those metals listed, ODS alloys exhibit exceptional properties such as Giga Pascal-level tensile strength (Ref 14), high temperature survivability (Ref 15), good creep resistance (Ref 16), reduced radiation damage (Ref 17, 18), and limited swelling and embrittlement after irradiation (Ref 19). Ferritic-based ODS alloys in particular have demonstrated high strengths in high-strain-rate situations (Ref 20). The potential advantage of the CS approach for ODS alloys is that the deposition is a solid-state bonding process, thus reducing the opportunity of grain growth and nano-oxide growth found in many current consolidating and joining techniques of ODS materials (Ref 21-25).

Maier et al. (Ref 26) have recently demonstrated the CS production of thin-walled (2 mm) tubes using gas-atomized powders that had a composition similar to ODS 14YWT (Fe-14% Cr, 3% W, 0.4% Ti, 0.2% Y, 0.01% O). Their success demonstrates the potential for mechanically alloyed steels with dispersed Y_2O_3 nanoparticles to be CS deposited. Prior to this report, Story et al. (Ref 13) specifically used LACS to successfully deposit ball-milled $Fe_{91}Ni_8Zr_1$ ODS material, which is the alloy studied in this work. The deposition efficiency for a high-pressure/high-temperature gas process was 8.1% with the simultaneous application of in situ laser heating; the deposition efficiency increased to 17.2%. The nano-scale oxides (less than 20 nm diameter) were retained in the deposited material (Ref 13). These two reports represent the current literature pertaining to CS deposition of ODS materials.

During the CS process, residual stresses in the deposits develop which have a dramatic influence on the physical properties, including the delamination of the deposit in extreme cases. The origins of these residual stresses are a result of individual particles impacting the surface peening of the already deposited material. This creates a plastic strain gradient and a resultant compressive residual stress on the surface. Mechanical equilibrium then dictates that a balancing tensile stress must develop elsewhere in the structure to compensate for the compressive stresses. As a result, compressive stresses are nominally located in the deposit with tensile stresses at or below the deposit/substrate interface. For CS of Al and Cu, the compressive to tensile residual stress trend has been observed and measured with hole drilling (350 μm thick deposits with -100 MPa compression stress at 100 μm thickness of Al 7075, + 20 MPa tensile stress 75 μm into the substrate of AZ31B-H24) (Ref 27), neutron diffraction (These deposits were 3 mm thick. For Cu on Cu, − 40 MPa compressive stress at 3 mm on the deposit, + 40 MPa tensile stress at the substrate–coating interface, and − 40 MPa compressive stress 2 mm into the substrate. For Al on Al, − 10 MPa compressive stress 1.5 mm on the deposit, + 20 MPa tensile stress at substrate–coating interface, and − 10 MPa compressive stress 2.5 mm into the substrate) (Ref 28, 29), in situ laser-based curvature devices (calculation of residual stress components from deposition and thermal effects) (Ref 30), and modified layer removal techniques (with 500-μm-thick coatings with − 500 MPa compressive stress reduced to − 50 MPa with substrate preheating) (Ref 31). Unlike conventional CS deposition, LACS can alter the surface residual stresses where the localized heating can yield a tensile state due to temperature gradients during cooling. Such thermal gradient-generated stresses are often found after laser heating of metals (Ref 32, 33). With these two competing mechanisms, a juxtaposed compressive and tensile residual stress generation in the same location at the same time offers a potentially rich area of investigation. To date, the influence of in situ laser heating during cold spray on residual stresses is unknown. Nevertheless, Yao et al. hypothesized that since LACS operates at lower surface temperatures than laser cladding or thermal spray, it should have less of an effect on thermal stresses (Ref 34).

This paper provides an initial investigation into the residual stresses generated by LACS, particularly for ferrous alloys. In this study, we use laboratory x-ray diffraction (XRD) to measure the residual stresses generated from the LACS deposition of a $Fe_{91}Ni_8Zr_1$ (at.%) ODS alloy onto a mild steel substrate. Specifically, we explore deposits done at surface temperatures of 650 and 950 °C. Prior work by Kotan et al. (Ref 35) revealed that the lower temperature is near the initial austenitization temperature for the alloy, while the higher temperature is above the completed austenite conversion temperature. To decipher how laser heating influences both material types as a function of the thermal input, residual stress measurements are also performed of laser only heated mild steel substrates.

Methods

Sample Fabrication

The ODS $Fe_{91}Ni_8Zr_1$ (at.%) alloy was produced by high-energy mechanical alloying in a Simolayer CM08 ball mill (Zoz, Wenden, Germany) with an 8-liter capacity, which yields $\sim$ 800 grams of milled powder. The starting elemental powders were all $-$ 325 mesh with respective purity levels: 99.9% iron, 99.8% nickel, and 99.5% zirconium. The appropriate quantities of each elemental powder were then loaded into a steel vial with 440 °C stainless steel balls, at a 10:1 ball to powder ratio, for high-energy ball milling in an argon atmosphere at 400 rotations per minute for 30 h yielding the desired composition. During this milling process, the powders were cooled to $-$ 25 °C to prevent powder (cold) welding.

The milled powder solid solution (Ref 36) was LACS deposited onto the mild steel substrates using a Gen III high-pressure cold spray system (VRC Metal Systems, Rapid City, SD) equipped with a WC–Co de Laval nozzle 200 mm in length, 2 mm diameter at the throat (35 mm from the start of the nozzle), and 6.3 mm diameter at the end of the nozzle (VRC Nozzle #60). The gas propellant was a nominal 75%/25% (vol.) mixture of He and N_2 gasses that exits the nozzle normal to the substrate surface at a gas pressure and temperature of 4.48 MPa (650 psi) and 600 °C. An LDM-4000-100 variable power (up to 4 kW) 940-nm wavelength diode laser (Laserline, Mülheim–Kärlich, Germany) was attached to the cold spray nozzle gas/powder applicator system at an offset of 29.1° that enabled the laser illumination of the space directly underneath the nozzle (Fig. 1). The laser was over-focused to create an assumed semi-Gaussian (top hat) power profile across the 8 mm laser spot size (Ref 32). A Mergenthaler unicolor pyrometer with a closed loop feedback system was used to control the power output of the laser to maintain a constant temperature at the deposition surface. Details concerning specific testing of this LACS system used may be found in the dissertation published by W. A. Story (Ref 37). All depositions were produced on cold-rolled AISI 1018 steel plates of 75 mm (width) × 300 mm (length) × 12.6 mm (thickness) (Grainger, Lake Forest, USA). The substrates were sanded with a P-80 grit abrasive paper, washed with soapy water, and then rinsed with isopropanol immediately prior to deposition.

During LACS, the sample surface temperature was set to be either 650 or 950 °C. In all cases, the laser spray gun assembly was translated across the substrate surface at an initial acceleration of 1000 mm/s^2 to attain a fixed velocity of 25 mm/s with each deposit produced on its own steel substrate. Each deposit was nominally 27 mm in length by
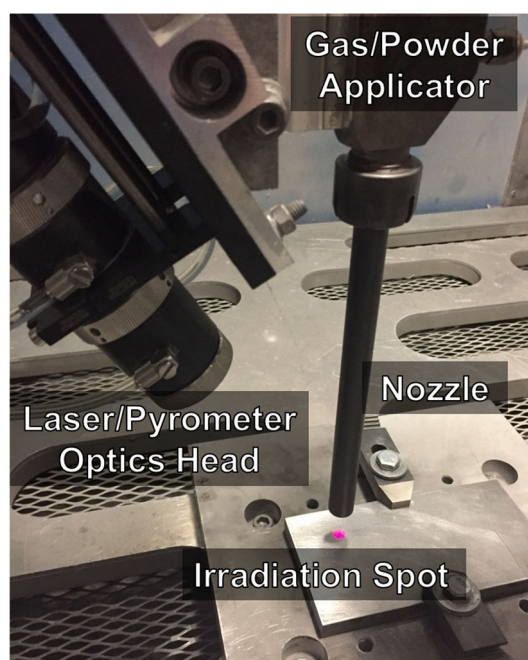

Fig. 1 Photograph of the LACS setup. In the top right, powder and heated gas combine to flow through the nozzle and exit perpendicular onto the substrate below. The laser is mounted to the powder/gas applicator, and a pilot light illuminates the surface underneath the nozzle indicating where the high-power infrared laser will irradiate during LACS. The pyrometer and laser share the same optics head

54 mm in width. An out-and-back raster pattern with 1.5 mm spacing between passes in the x–y plane (longitudinal–transverse) was used for all deposits (Fig. 2). Six layers were deposited in the vertical (z) direction with the final thickness of the deposit being dependent upon the deposition characteristics of the LACS conditions.

Laser Heating Responses During LACS Deposits

The temperature control system for the LACS instrument governs the surface temperature at both high and low frequency adjustments to the laser power (Fig. 3). The laser and attached pyrometer are coupled in a closed feedback loop that adjusts the laser power in order to keep a constant temperature on the sample surface, as shown in Fig. 1. Adjustments are made within millisecond (ms) durations. Whether it be laser irradiation only (for the substrate only study) or LACS (for the ODS powder deposition), all recorded temperatures reached steady state in less than 20 ms. Deviations from the measured temperature were not greater than 1 °C. During LACS, the gas was heated with the powder feeding initiated before the laser was activated. When the laser was turned on, it was found that the power initially spiked followed by a subsequent power decay before the laser movement started. This power variation is caused by the heating and feedback loop with the

Fig. 2 (a) Photograph of multi-pass and layered ODS material deposited by LACS at 950 °C. (b) Photograph of laser-irradiated 1018 steel substrate. The oxidation lines from the elevated temperature indicate the path of the laser (c) Raster geometry of the multilayered spray with movement of 27 mm in the x_1 direction and 1.5 mm in the x_2 direction with 37 passes for a total of 54 mm in the x_2 direction
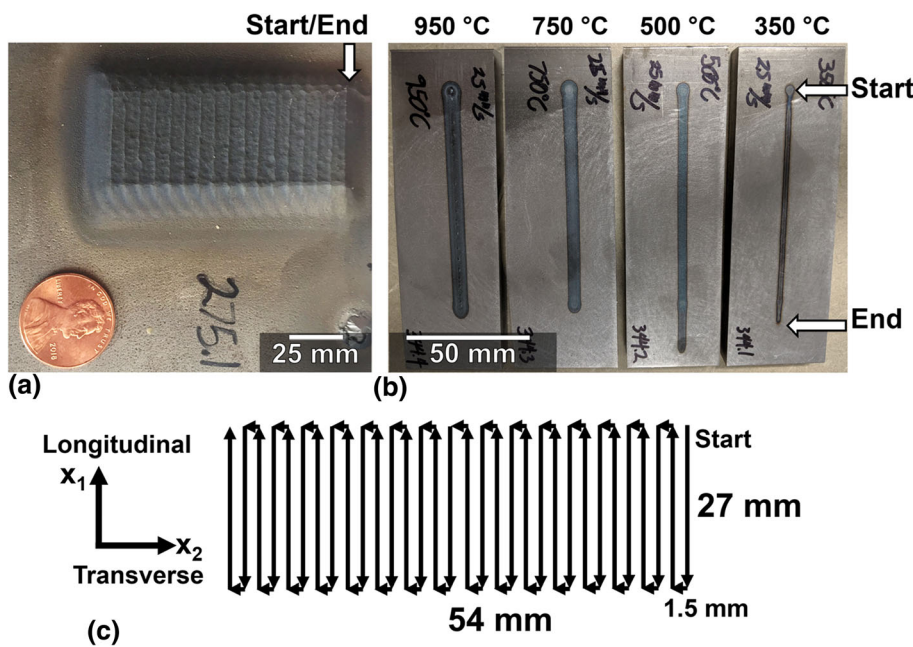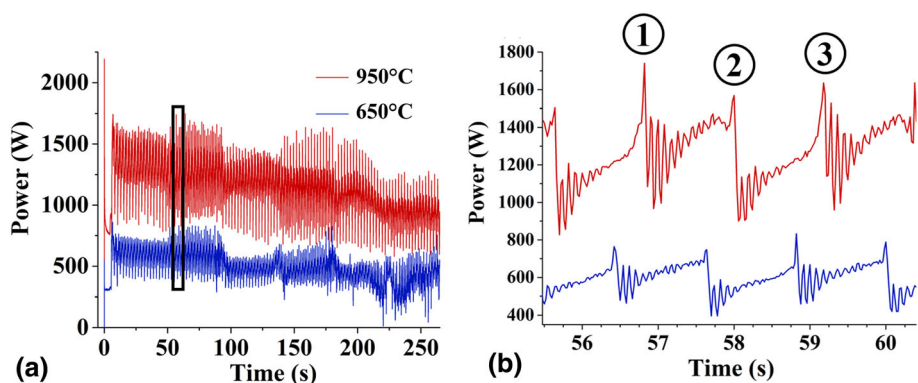
Fig. 3 (a) Laser power outputs of LACS during deposition of six layers of ODS $Fe_{91}Ni_8Zr_1$. (b) Magnified section showing the first few raster sections of the second indicated by the box in (a) and zoomed in. The periodic changes of laser power correspond with the raster motion of the laser

pyrometer when the laser is stationary, but this dramatic change ceased once the laser traversed the surface. Since a change in laser raster direction occurs with each pass, this oscillatory power spike can be seen in the power vs. time scans shown in Fig. 3. Each raster took slightly longer than one second because of the acceleration of the spray gun assembly. When the raster was away from the starting location (i.e., point 1 in Fig. 3b), the laser moves onto a point on the substrate at a lower temperature, and the laser power then increases to compensate. After the nozzle laser apparatus completes the raster, it moves 1.5 mm laterally down the substrate (i.e., point 2 in Fig. 3b) and then returns along the same direction it came from (i.e., point 3 in Fig. 3b). The time necessary to stop the spray gun assembly and turn around was sufficient for the laser to heat the substrate at relatively the same spot and, as a result, the laser power decreased sharply until the laser moved again in the raster direction at which time the power increased again. It was noted that the power required for

the apparatus to move away from the edge of the starting location was always larger than the power required to come back to that edge.

After a raster area was completed, the laser began the next sequence of deposition by reversing the direction and rastering back to its starting location and depositing the new layer. At the end of each layer, the robotic system that controls the spray and laser assembly was advanced 0.1 mm in the z direction to match the height that was deposited on the surface in the prior raster. The average power output gradually decreased with each new layer, indicating that less power was required to keep the temperature equal.

Laser Heating Responses of the Mild Steel Substrate

For comparison, a series of laser-heating-only experiments were investigated by a single laser heating pass on 1018 steel (0.18 wt.% C, < 0.75 wt.% Mn, < 0.05 wt.% P and

< 0.05% S) substrates (Fig. 2b). These experiments were carried out over a larger temperature range: 350, 500, 750, and 950 °C. The pyrometer was used to control the surface temperature throughout. The single laser heating passes were 100 mm long and done at speeds of either 5 or 25 mm/s. All runs were done on separate substrates with dimensions of 50 mm (width) × 300 mm (length) × 12.6 mm (thickness) so that no one substrate had multiple single laser runs on its surface. There was an approximate 1-2 seconds (user controlled) gap between turning the laser on and starting the movement of the nozzle. The path of the laser irradiation treatment is easily identified by the oxidation marks.

Figure 4 shows the surface temperature and recorded laser power outputs associated with the laser-only scans on these substrates. When the laser started, the power spiked to its maximum output and then decreased exponentially to quickly reach and maintain the set point temperature, as was previously noted in the LACS of the ODS powder. As the laser began to move, it encountered the substrate surface, which was at a lower temperature, resulting in a rapid power increase to establish a constant temperature set point. With the laser moving at 5 mm/s, this laser jump was relatively small and varied between 464 and 560 W for the lower bound 350 °C surface condition and 748-856 W at the upper bound 950 °C surface condition. After reaching a

steady velocity, the power remained steady for the duration of the run. When the laser velocity was increased to 25 mm/s, this jump increased from 496 to 1204 W at 350 °C and 1148-2688 W at 950 °C. As would be expected, higher temperatures required a higher steady-state power output. When the velocity of the laser was increased, a higher power output was required in order to maintain the same temperature. The corresponding linear heat input values are shown in Fig. 4d, which reveals that at all temperatures tested, the linear heat input was higher at 5 mm/s than at 25 mm/s.

Characterization

Surface residual stress was measured using an iXRD (Proto Manufacturing, MI, USA) x-ray residual stress diffractometer. The residual stresses parallel to the traversal path of the deposit were measured (the x_2 direction as described in Fig. 2). These measurements were collected using a Cr k_α x-ray source (wavelength λ = 2.291 nm, 1 mm diameter circular beam) and employed the d versus $\sin^2(\psi)$ approach in conjunction with elliptical data fitting to determine the in-plane (σ) (in conjunction with the directions x_1 and x_2 directions, see Fig. 5) residual stress components at each point. The hkl plane measured was {211} which has a Bragg angle of 156.31° and d-spacing, d_0 = 1.1704 Å. The
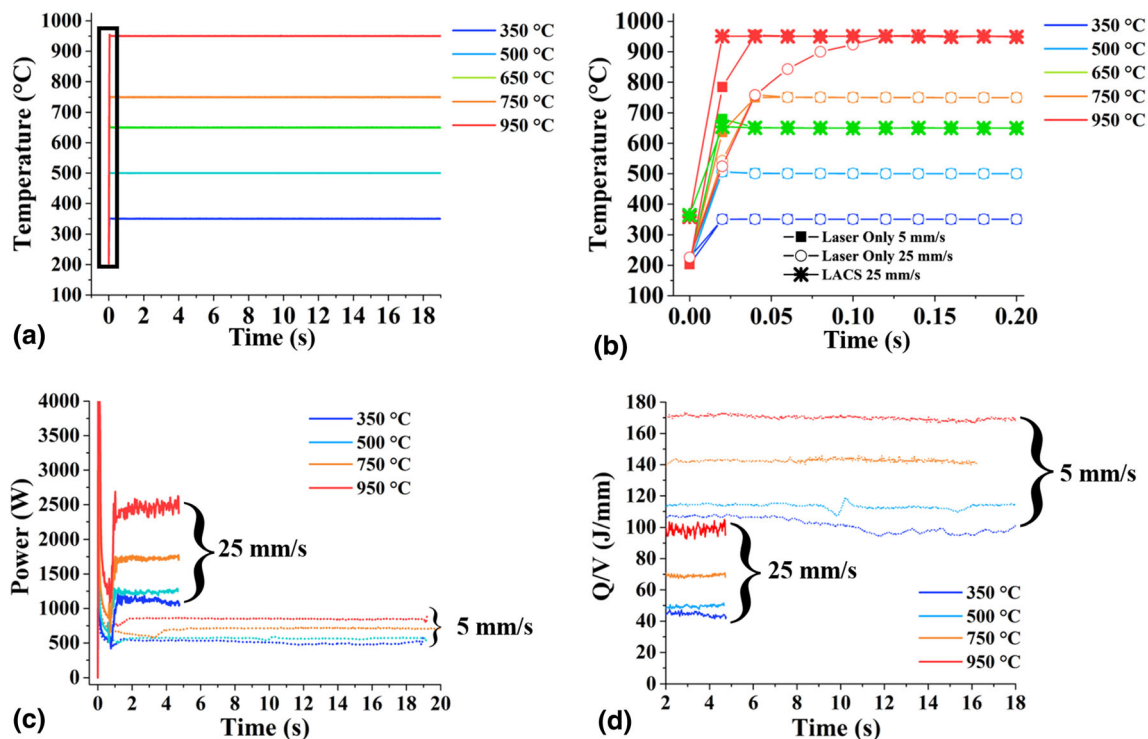

Fig. 4 (a) Temperature profiles of the sample surface during laser irradiation and LACS as a function of time. (b) A zoomed in portion of (a) of the first 20 ms. (c) Power outputs of the laser at different set surface temperatures and velocities. (d) Linear heat input (Q/V) as a function of spray gun velocity, of different temperatures and speeds of laser irradiation
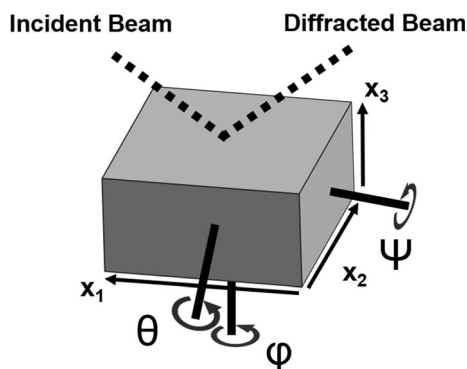
Fig. 5 Schematic of the orientations of XRD in the case of determining residual stresses. The directions θ, φ, and ψ are orthogonal to each other. The φ angles were in increments of 90° as residual stresses were taken parallel to either the x_1 or x_2 directions (Fig. 2)

system alignment was checked using a stress-free iron powder (residual stress of 0 ± 14 MPa) and high-stress steel standard (residual stress of -474 ± 35 MPa) for each set of measurements. Two detectors, fixed on opposite sides of the x-ray source (to simultaneously measure negative and positive ψ tilts), were incrementally rotated in the ψ orientation to measure d-spacing as a function of $\sin^2(\psi)$ as illustrated in Fig. 5.

Previously derived equations may be used to determine the strain in the material (Ref 38). When Hooke's law is applied:

$$\sigma_{ij} = C_{ijkl}\epsilon_{kl}, \tag{Eq 1}$$

determined strain may be written as a function of stress and materials properties:

$$\epsilon_{\phi\psi} = \frac{(d_{hkl})_{\phi\psi} - d_0}{d_0} = \frac{1+v}{E}\left(\sigma_\phi \sin^2 \psi\right) - \frac{v}{E}(\sigma_1 + \sigma_2), \tag{Eq 2}$$

where σ_φ is the surface stress at angle φ, E is the modulus of elasticity, v is the Poisson's ratio, and σ_1 and σ_2 are the principal stresses. Equation 2 then may be written as:

$$d_\psi = \frac{1+v}{E}d_0\sigma_\phi \sin^2 \psi - \frac{v}{E}(\sigma_1 + \sigma_2)d_0 + d_0. \tag{Eq 3}$$

The variation in the plane spacing with $\sin^2 \psi$ is linear, with the slope represented as:

$$m = \frac{1+v}{E}d_0\sigma_\phi. \tag{Eq 4}$$

From the known materials properties and the slope of d-spacing and $\sin^2(\psi)$, residual stress can then be calculated. This is known as the $\sin^2(\psi)$ method of determining residual stress through XRD (Ref 38). The method of calculating residual stress, as well as machine alignment through stress-free and pre-stressed material, has been

standardized (see ASTM: E915-19 and ASTM: E2860-12). For determining residual stress, the elastic constant that was used was:

$$\frac{E}{1+v} = 169 \text{ GPa}. \tag{Eq 5}$$

In the case of compressive in-plane stresses, the measured d-spacing will decrease with increasing $\sin^2(\psi)$, generally in a linear trend, with the opposite effect occurring for tensile stress conditions. In a sample portion with no stresses in the surface regions, the measured d-spacing remains constant at all ψ angles, i.e., zero gradient.

After completion of the residual stress measurements, the samples were sectioned perpendicular to the raster direction of the LACS depositions (cross sections) into sizes of approximately 4 cm³ and hot mounted using Bakelite with carbon fillers (Polyfast, Struers, Cleveland, OH, USA). Sample surfaces were metallographically prepared by systematic grinding with coarse (320 grit) to fine (600, 1200 grits) SiC paper, polishing using diamond suspensions with particle sizes 3 μm and 1 μm, and vibration polishing using 0.05 μm alumina. Grain structures of the laser-irradiated samples were revealed through etching (2 vol% nitric acid, 98 vol% ethanol) and analyzed using optical microscopy (Inverted Metallurgical Microscope, AmScope, CA, USA) and ion contrast imaging with an Quanta dual beam focused ion beam (Thermo-Fisher Scientific, MA, USA).

Average microhardness testing of the LACS ODS $Fe_{91}Ni_8Zr_1$ deposits was done on the cross sections using an automated Buehler's (Vickers Hardness) Tukon 1202 model microhardness tester (Clemex, Quebec, Canada) employing a load of 50 g force and a dwell time of 10 s. Fifteen to eighteen measurements were made across the coating in the longitudinal (x_1) and through thickness directions. Care was taken while performing these indentation impressions to avoid defects and visible pores.

Results and Discussion

Residual Stresses in ODS Deposits Produced by LACS

Residual stress results for the measurements on the surfaces of the LACS deposits are indicated in Fig. 6. For both the 650 and 950 °C deposition conditions, the d versus $\sin^2(\psi)$ plots reveal negative slopes, indicative of compressive stresses. While the in-plane stresses were uniformly compressive, the range (difference of the maximum and minimum) of the surface residual stresses varied across the deposits for both deposition temperatures by about 300 MPa. The transverse (x_2) component of the residual

Fig. 6 (a) d-spacing versus $\sin^2(\psi)$ plots of the transverse (x_2) component from XRD measurements taken at single points on the ODS $Fe_{91}Ni_8Zr_1$ LACS deposits at surface temperatures of 650 °C and (b) 950 °C. These points, with location coordinates indicated in the graph legends, are arbitrarily taken at different places on the deposits. The surface residual stresses determined from the respective plot gradients are indicated in the graph legends. Solid lines represent $\psi < 0$. Broken lines represent $\psi > 0$. (c) Maps of surface residual stresses from deposits made at surface temperatures of 650 °C and (d) 950 °C with the horizontal axes representing distances in the longitudinal (x_1) direction and the vertical axes representing distances in the transverse direction (x_2). The dots on the maps represent actual measured locations. The (0,0) point represents the top of the LACS pad closest to the starting location. Error is ± 20 MPa or less
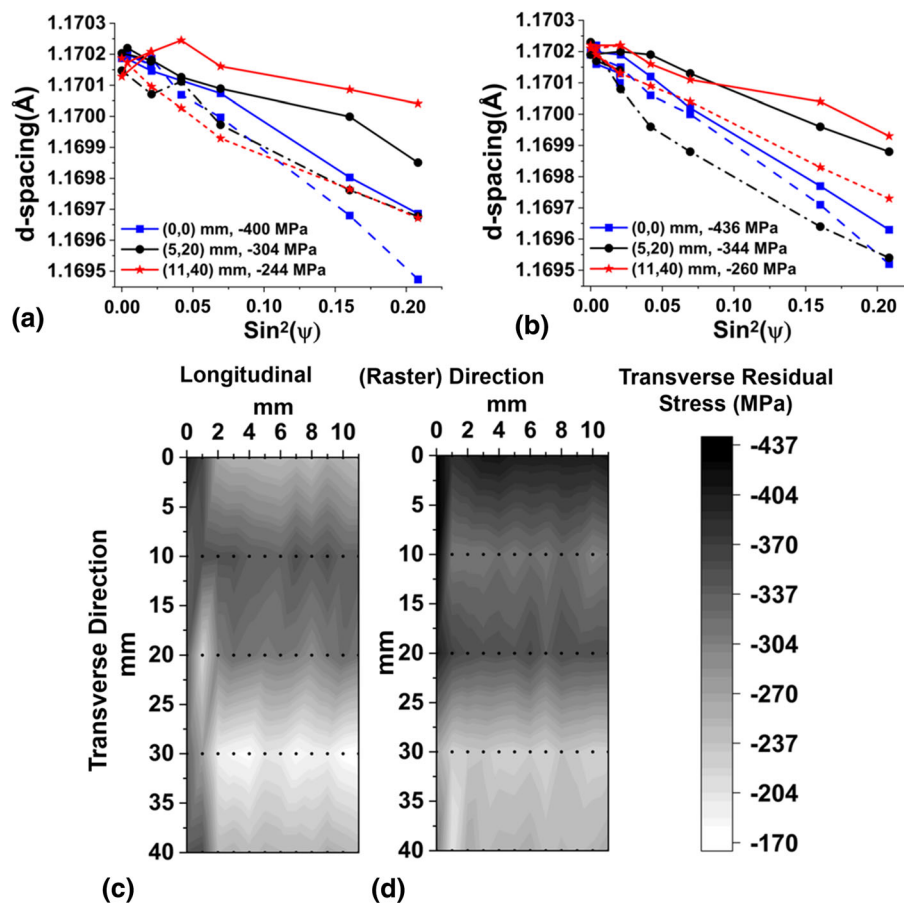
stress does not substantially change in the longitudinal direction (raster direction, x_1). However, the residual stresses were more compressive at the start of the deposit and become less compressive further from the start in the transverse (x_2) direction. Since no tensile residual stresses were found in either LACS deposit, this confirms that the compressive residual stress-causing mechanism of shot peening from the cold spray process is the dominant mechanism that overcomes the tensile residual stresses created from thermal gradients created by the point heat source of the laser. Nevertheless, this change may also be a result from the surface cooling faster than the interior pulling this section of the sample into a compressive stress state. Further experiments involving slit compliance, neutron diffraction, and/or synchrotron x-ray diffraction will be used in the future to look at the evolution of these stresses with depth.

Deposit Microstructures and Hardness Produced by LACS on ODS $Fe_{91}Ni_8Zr_1$

The influence of the in situ laser heating was evident in both the deposition characteristics and in the microstructures of the LACS-deposited materials. The measured deposition efficiency (dividing the mass change of the substrate by the mass change in the powder feeder) was 7.03% and 32.4% for the 650 °C and 950 °C surface temperatures, respectively. The interface between the substrate and the deposit appeared well bonded for both conditions, but the deposited microstructures were notably different (Fig. 7a and 6b). This difference is most apparent when considering the deposit-on-deposit interfaces between the layers (Fig. 7c and d). As shown in Fig. 7c for the 650 °C deposit, at approximately half the depth of the deposit, pores and debonded layers, which are tens of microns in width, are evident. It is worth noting that this metallographic sectioning was done post-residual stress measurements; thus, it is unclear if the sectioning process itself caused the debonding or if the debonding was already present in the material. Nonetheless, the 650 °C deposited sample had a section of the deposit delaminate from the substrate during sectioning providing a qualitative indication of abundant residual stress present in the deposit.

In addition to pores and debonding noted in the lower magnified images between the LACS deposits (650 and 950 °C), their microstructures were also different. Prior to deposition, the ODS powder has previously been reported to be composed of nanocrystalline grains created from the high-

Fig. 7 (a) Cross-sectional optical micrographs of LACS deposits of ODS $Fe_{91}Ni_8Zr_1$ done at mild steel substrate–deposit interface at constant temperatures of 650 °C and (b) 950 °C. (c) Lower-magnification images showing multi-layer interfaces internal to the deposit at 650 °C, (d) 950 °C
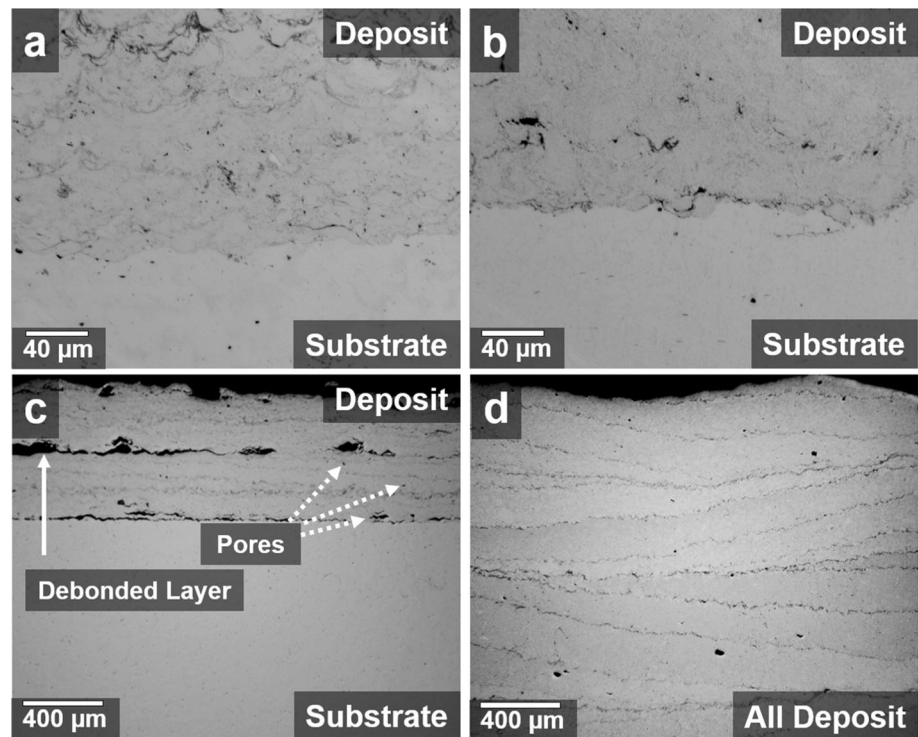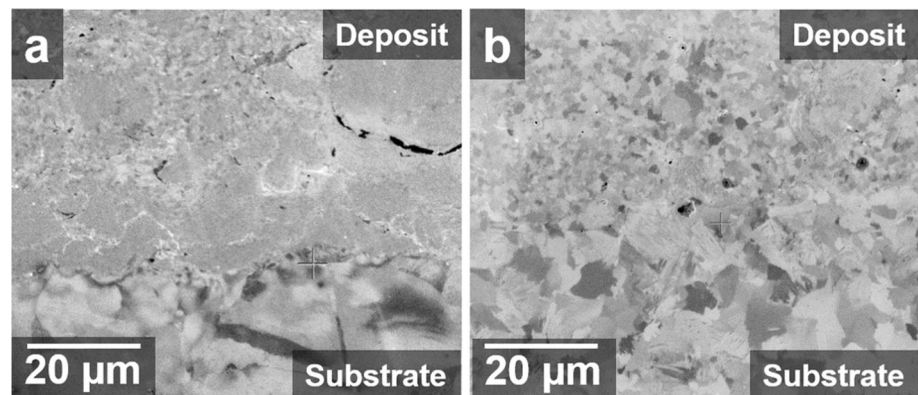

Fig. 8 Focused ion image contrast micrographs of single-pass LACS of ODS $Fe_{91}Ni_8Zr_1$ with surface deposition temperatures of (a) 650 °C and (b) 950 °C

energy ball milling process of the constituent powders (Ref 36, 39). Focused ion contrast images (Fig. 8) revealed that the ferrite grain size for the 650 °C surface temperature deposit exhibited a binomial grain size distribution, with some isolated regions retaining a fine grain size (sub-micron) while other regions being coarsened in the micron size regime (Fig. 8a). At the 950 °C surface temperature, all the ferrite grains have grown (microns in sizes) with some grains being particularly large suggesting abnormal grain growth.

These grain coarsening observations are aligned with a related in situ heating study of these ODS powders (Ref 35). Here, XRD Scherrer analysis showed that the grains coarsen with temperature. Above 700 °C, focused ion contrast images revealed the beginning of abnormal grain growth and the loss of the nanocrystalline state. In another

study, Story et al. used electron backscattered electron diffraction analysis and confirmed grain growth in LACS deposit of ODS $Fe_{91}Ni_8Zr_1$ (Ref 13). As would be expected, the increase in ferrite grain size leads to a reduction in measured hardness for the two deposits. The sample deposited at 650 and 950 °C had an average Vickers hardness of 598 ± 56 and 293 ± 38, respectively (Fig. 9).

Residual Stresses in the Mild Steel Substrate

The residual stresses measured on the surface of the 1018 steel substrate prior to laser irradiation are shown in Fig. 10a. Being cold worked and sanded (see experimental detail section), the substrates contained a compressive residual stress state. In the direction of the laser irradiation,

the average compressive stresses were -227 MPa. The average compressive residual stress in the transverse direction (x_2) was -196 MPa, revealing a near-equiaxed residual stress in the pre-coated substrate. The residual stress profile in Fig. 10b shows the transverse component (x_2) of the in-plane surface stress in the substrate over the laser track when the surface temperature was set at 350 °C with the laser moving at a velocity of 25 mm/s. Figure 10b reveals the existence of tensile, zero, and compressive stress regions at discrete locations over the profile (labeled 1, 2, and 3). The d-spacing versus $\sin^2(\psi)$ relationships for these three points are shown in Fig. 10c. The residual
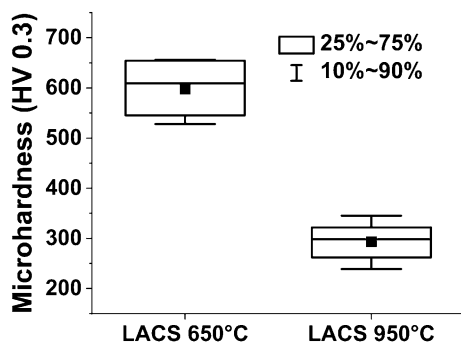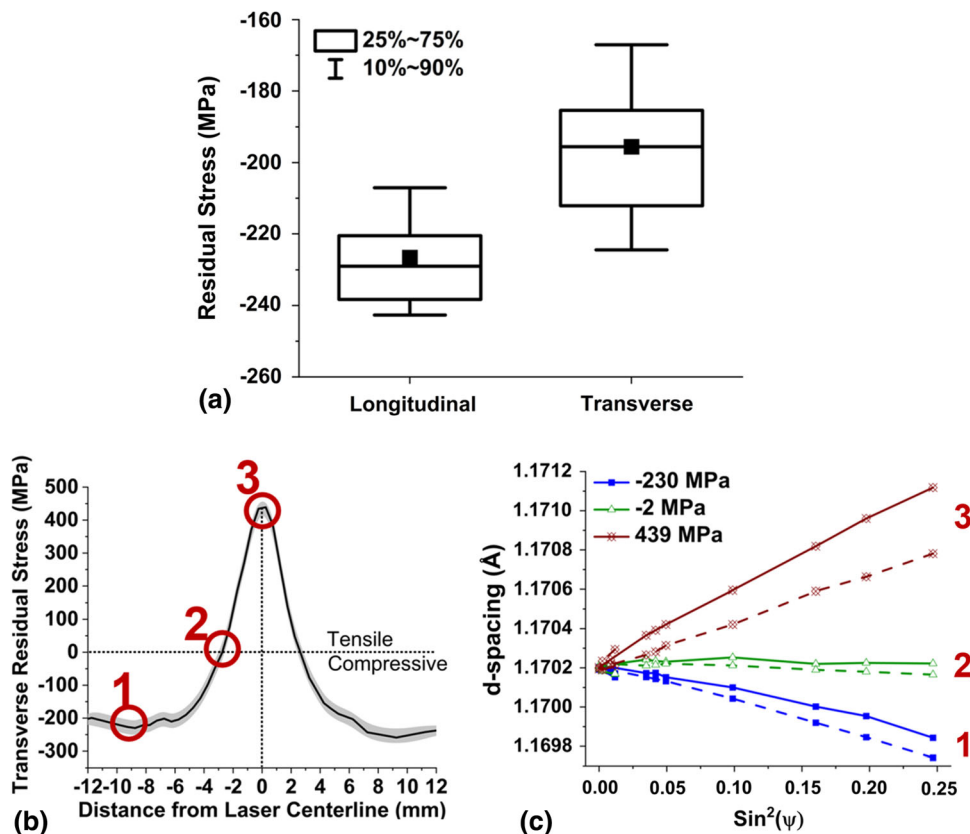
Fig. 9 Box-and-whisker plots of hardness results of the cross-sections of LACS of ODS $Fe_{91}Ni_8Zr_1$ deposited at surface temperatures of 650 °C and 950 °C

stresses are compressive at distances further than 3 mm from the centerline of the laser track in both the transverse (x_2) and longitudinal (x_1) directions. The residual compressive stresses increase in magnitude until 8 mm from the laser centerline where the residual stress becomes similar to that measured in the base plate. Tensile residual stresses are observed at the laser scan center line.

With increasing surface temperature and/or the laser speed, Fig. 11 indicates changes in the width and shape of the tensile parts of the residual stress profiles on the laser scan centerline. Above surface temperatures of 750 °C, the distribution of residual stresses formed an "M-shaped" profile with the tensile maxima now at the outer regions of the laser spot and a lower level of tensile residual stress at the center line. This profile was well defined for the 5 mm/s pass at 750 °C, but became less defined at 950 °C. For the 25 mm/s laser speed, the residual stress magnitudes become larger than those observed for 5 mm/s at all temperatures. In addition, the development of the M-shaped profile begins at a nominal surface temperature of 500 °C and is retained to 750 °C. At 950 °C, the profile evolves into a "W-shaped" profile.

These residual stress profiles result from the thermal gradients and microstructural evolution of the 1018 steel with temperature. Localized heating during laser welding or heat treatment generates tensile stresses in the central

Fig. 10 (a) Box-and-whisker plots of surface residual stresses determined on the AISI 1018 steel substrate surface prepared (but prior to LACS process) with XRD (40 scans each). The directions longitudinal (x_1) and transverse (x_2) correlate with the intended laser irradiation and LACS treatments shown in Fig. 1. The black square in the center of each box denotes the mean of the measured stress. (b) Transverse (x_2) residual stress component across the laser track with the sample temperature set at 350 °C and moving at a velocity of 25 mm/s. The light gray region shows the estimated error. Residual stresses were calculated from the measured d-spacing versus $\sin^2(\psi)$ plots, examples of which are shown in (c). The points labeled 1–3 in (b) correspond to the d-spacing measurements in (c). The solid lines represent $\psi < 0$. Broken lines represent $\psi > 0$
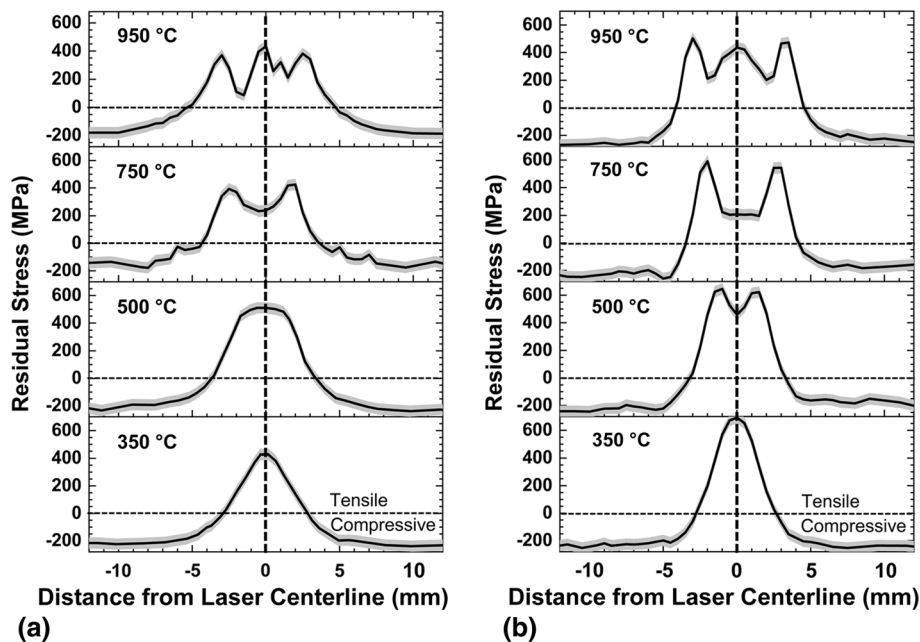
Fig. 11 Longitudinal (x_1) component of the surface residual stress determined with XRD across laser irradiation tracks at different surface temperatures and velocities of (a) 5 mm/s and (b) 25 mm/s. The light gray region shows error

parts of the heated area which are compensated by compressive regions outside this heated region (Ref 32, 40). This behavior is clearly seen for the 350 °C and 500 °C surface temperatures in Fig. 11. Once the steel reaches a high enough temperature, it begins to transform from the existing ferrite and pearlite microstructure to a ferrite and austenite microstructure (A_1 transition) and then finally to solely austenite (A_3 transition). For 1018 steel, the key transformation temperatures are $A_1 = 710$ °C and $A_3 = 836$ °C (Ref 41). If the heating and cooling of the steel are sufficiently rapid into and out of the austenite phase field, martensite will then form. The presence of martensite would correlate with decreased tensile or even compressive stresses even though thermal gradients would produce high tensile stresses (Ref 42). The net effect of the spatially different cooling rates caused by a thermal gradient combined with expansion caused by the diffusionless phase transformation reduced the tensile residual stress at the center of the laser pass, thus producing the M-shaped profile. The M-shaped profile is consistent with other single-pass modeling and measurement of residual stress of laser treatments of similar ferrous alloys but of different compositions (Ref 40, 43, 44).

Microstructures and Hardness of Laser-Irradiated Mild Steel Substrate

Both hardness tests and optical micrographs, as shown in Fig. 12, reveal martensite within the heated zone for the higher surface temperature deposits. At the 750 °C and 950 °C laser-irradiated surface temperatures, the hardness increases substantially, from 225 to 400 HV, as shown in

Fig. 12a, and is indicative of this martensite formation. These hardness values and respective spatial profiles correspond well to the cross sections of the deposits and their associated dips in the tensile residual stresses, as described in "Residual Stresses in the Mild Steel Substrate" section. Additionally, etched micrographs revealed two zones. Zone 1, which is closest to the surface (Fig. 12c), has an abundance of martensite (indicated by the arrows in that micrograph) and zone 2, which is below the surface, has a mixture of martensite and ferrite (with the martensite being the indicated arrows pointed at the laths in the microstructure). In the 750 °C condition, a mixture of martensite and ferrite was found.

As the laser moved at the faster rate, a higher thermal gradient would be produced, which in turn would generate larger residual tensile stresses. The compressive dip in the center part of the "M" shape would then become more pronounced at higher velocities. At 500 °C with a 25 mm/s laser raster speed, a small depression in the residual stress is observed (Fig. 11b). This temperature is below the A_1 transition, and so the formation of austenite and then martensite would not be expected; nevertheless, the residual stress profile would suggest the phase transformation. This unexpected result is explained by the laser spot profile in the irradiated region. The nominal profile for the overfocused laser was assumed to have a top hat shape (Ref 32), but these residual stress findings would suggest that the laser profile still retained some Gaussian shape distribution. By having a Gaussian distribution, spatially some regions will be exposed to a higher heat input from the laser than other regions, even though the overall average heat would be given by the single-spot pyrometer measurement. These

Fig. 12 (a) Vickers hardness maps of the sample cross sections for laser scans done at a velocity of 25 mm/s. Cross sections were taken at 50 mm (halfway) into the scan. Hardness tests on average were taken approximately 50 μm from the top surface. (b) Zoomed in photograph of the 950 °C laser irradiation track. (c) Optical micrograph of an etched portion of the cross section of steel irradiated at 750 °C with (d) zoomed in on the surface. (e) Optical micrograph of an etched portion of the cross section of steel irradiated at 950 °C with (f) zoomed in at the surface. The micrographs revealed two zones. Zone 1, which is closest to the surface, has an abundance of martensite (indicated by the arrows) and zone 2, which is below the surface, has a mixture of martensite and ferrite (martensite indicated by arrows pointed at the laths in the microstructure)
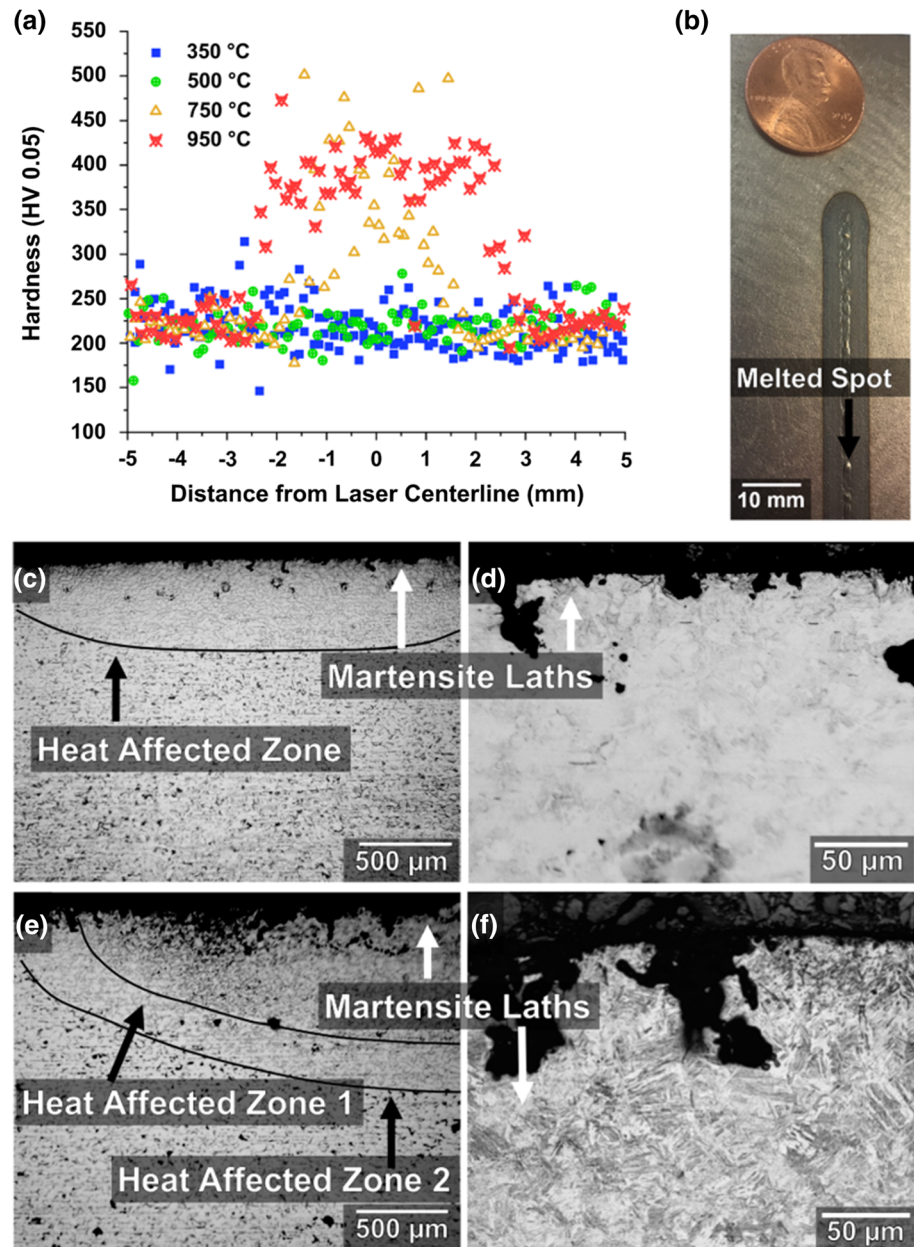
"hotter" regions would then exceed the A_1 temperature such that a small amount of austenization occurred. Upon cooling, some martensite transformation occurred that caused the dip in residual stress. Although the average temperature from the laser was 500 °C, the pyrometer only measures an average temperature over the region and demonstrates some of the current technical challenges of uniform laser heating. The reason for the "W" shape in the 950 °C surface condition is not completely clear, but some evidence for localized melting (Fig. 12b) in the top 200 microns of the center of the laser pass was observed and may be responsible for this change. This localized melting again could be explained by a Gaussian power distribution across the laser spot (and therefore temperature) profile imparted by the laser to the substrate.

Comparing Residual Stresses Responses

In the CS deposits, a compressive residual stress was measured. In contrast, the mild steel substrate revealed a tensile stress after heating. Nevertheless, the tensile profile shape changed with either an increase in temperature and/ or laser raster speed for the substrate through the contribution of a smaller absolute value of compressive stress within the laser heated profile. These changes were explained by a phase transformation in the steel via the

subsequent presence of martensite. Thus, could a similar compressive stress mechanism be present in the ODS deposit?

In a prior report for this ODS alloy (Ref 35), an in situ XRD study confirmed that a face-centered cubic (austenite) peak begins to form at 650 °C; however, the ferric body-centered cubic peak was still present (albeit it in lower phase fraction) up to 900 °C. These two temperatures dictated the temperatures chosen for the deposit. Nevertheless, this phase change did not dramatically influence the residual stress profile. Previous chemical analysis of the ODS alloy revealed carbon content less than 0.1% (Ref 20). Because of such a low carbon content, it is unlikely that martensite formed in this powder alloy, which was confirmed by a lack of its microstructural presence in the micrographs. Thus, the compressive stress mechanism in the LACS deposit is not a result of martensite formation, as observed in the substrate.

Rather, the compressive stresses are believed to be either from the intrinsic cooling behavior of the deposit itself or, more likely, intrinsic effects from CS deposition. Even though the surface temperature for the ODS deposit was quite high, where such temperatures were sufficient for the mild steel substrate to generate tensile residual stresses, it is possible that the surface of the LACS deposit cools more rapidly than the heated interior, thus pulling the surface into compression. Likely more probable is the existence of compressive stress mechanisms in CS. One compressive stress generation mechanism is created from each individual particle because of the extreme deformation it undergoes by virtue of the supersonic velocities and subsequent impact onto the substrate (Ref 45, 46). The other compressive stress generation mechanism is the shot peening effect where the accelerated particles hit the surface, but do not stick, and ricochet off creating a peening effect (Ref 46). The low deposition efficiency confirms that this effect is present as not all powders adhere to the deposit. These compressive mechanisms are sufficient to overcome any tensile stress generated by the thermal gradients created by the laser input heating.

Conclusions

This article has provided an initial investigation into the residual stresses produced by the LACS process on ferrous alloys. We observed compressive surface residual stresses on multilayered LACS deposits of ODS $Fe_{91}Ni_8Zr_1$ deposited at 650 °C and 950 °C. These stresses were all compressive but were not uniform in magnitude across the deposit. In comparison, single-layer passes on the mild steel substrates used for the LACS deposition showed

tensile residual stresses and martensite formation at higher surface temperatures.

A series of residual stress tests were performed on laser-irradiated AISI 1018 substrate at velocities of 5 mm/s and 25 mm/s and temperatures between 350 and 950 °C. The laser-irradiated samples under 500 °C had tensile residual stresses on the laser track with the stress maximum at the laser centerline caused by thermal gradients within the laser spot. An increase in velocity increased this tensile residual stress. Laser temperatures at 750 °C had an "M"-shaped peak caused by martensitic phase transformations, and laser temperatures at 950 °C created a "W"-shaped peak caused by both surface melting and solidification followed by martensitic phase transformations. This was confirmed through microstructural and hardness characterizations.

Considering the unlikelihood of the ODS material to create martensite, the compressive surface residual stresses are plausibly caused by both the extreme plastic deformation of the particle upon impact onto the substrate and a peening effect from particles that strike but do not adhere to the deposit. These compressive stress-generating mechanisms were sufficient to overcome thermal gradient generating tensile stress behavior nominally observed with laser heating only effects.

References

1. A.P. Alkhimov, A.N. Papyrin, V.F. Kosarev, N.I. Nesterovich, M.M. Shushpanov, Gas-Dynamics Spraying Method for Applying a Coating, ed., Papyrin, Anatoly Nikiforovich, 1994
2. R.N. Raoelison, C. Verdy, and H. Liao, Cold Gas Dynamic Spray Additive Manufacturing Today: Deposit Possibilities, Technological Solutions and Viable Applications, *Mater. Des.*, 2017, **133**, p 266-287
3. V. Champagne and D. Helfritch, The Unique Abilities of Cold Spray Deposition, *Int. Mater. Rev.*, 2016, **61**(7), p 437-455
4. A.I. Katsamas and G.N. Haidemenopoulos, Laser-Beam Carburizing of Low-Alloy Steels, *Surf. Coat. Technol.*, 2001, **139**(2–3), p 183-191
5. M. Bray, A. Cockburn, and W. O'Neill, The Laser-Assisted Cold Spray Process and Deposit Characterisation, *Surf. Coat. Technol.*, 2009, **203**(19), p 2851-2857
6. R. Lupoi, A. Cockburn, C. Bryan, M. Sparkes, F. Luo, and W. O'Neill, Hardfacing steel with nanostructured coatings of Stellite-6 by supersonic laser deposition, *Light Sci. Appl.*, 2012, **1**(5), p 1-6
7. B. Li, Y. Jin, J. Yao, Z. Li, and Q. Zhang, Solid-state fabrication of WCp-reinforced Stellite-6 composite coatings with supersonic laser deposition, *Surf. Coat. Technol.*, 2017, **321**, p 386-396
8. E.O. Olakanmi, M. Tlotleng, C. Meacock, S. Pityana, and M. Doyoyo, Deposition Mechanism and Microstructure of Laser-Assisted Cold-Sprayed (LACS) Al-12 wt% Si Coatings: Effects of Laser Power, *JOM*, 2013, **65**(6), p 776-783

9. D.K. Christoulis, M. Jeandin, E. Irissou, J.-G. Legoux, W. Knapp, Laser-Assisted Cold Spray (LACS), Nd YAG Laser, 1 ed., I. Open, Ed., 2012, pp. 59-96

10. J. Yao, L. Yang, B. Li, and Z. Li, Beneficial Effects of Laser Irradiation on the Deposition Process of Diamond/Ni60 Composite Coating with Cold Spray, *Appl. Surf. Sci.*, 2015, **330**, p 300-308

11. J. Morimoto, T. Onoda, Y. Sasaki, and N. Abe, Improvement of Solid Cold Sprayed TiO_2–Zn Coating with Direct Diode Laser, *Vacuum*, 2004, **73**(3–4), p 527-532

12. M. Kulmala and P. Vuoristo, Influence of Process Conditions in Laser-Assisted Low-Pressure Cold Spraying, *Surf. Coat. Technol.*, 2008, **202**(18), p 4503-4508

13. W.A. Story, D.J. Barton, B.C. Hornbuckle, K.A. Darling, G.B. Thompson, and L.N. Brewer, Laser Assisted Cold Spray of Fe–Ni–Zr Oxide Dispersion Strengthened Steel, *Materialia*, 2018, **3**, p 239-242

14. M.J. Alinger, G.R. Odette, and G.E. Lucas, Tensile and Fracture Toughness Properties of MA957: Implications to the Development of Nanocomposited Ferritic Alloys, *J. Nucl. Mater.*, 2002, **307–311**, p 484-489

15. L. Straßberger, A. Chauhan, T. Gräning, S. Czink, and J. Aktaa, High-Temperature Low-Cycle Fatigue Behavior of Novel Austenitic ODS Steels, *Int. J. Fatigue*, 2016, **93**, p 194-200

16. M.C. Brandes, L. Kovarik, M.K. Miller, G.S. Daehn, and M.J. Mills, Creep Behavior and Deformation Mechanisms in a Nanocluster Strengthened Ferritic Steel, *Acta Mater.*, 2012, **60**(4), p 1827-1839

17. S. Rogozhkin, A. Bogachev, O. Korchuganova, A. Nikitin, N. Orlov, A. Aleev, A. Zaluzhnyi, M. Kozodaev, T. Kulevoy, B. Chalykh, R. Lindau, J. Hoffmann, A. Möslang, P. Vladimirov, M. Klimenkov, M. Heilmaier, J. Wagner, and S. Seils, Nanostructure Evolution in ODS steels Under Ion Irradiation, *Nucl. Mater. Energy*, 2016, **9**, p 66-74

18. R. Schäublin, A. Ramar, N. Baluc, V. de Castro, M.A. Monge, T. Leguey, N. Schmid, and C. Bonjour, Microstructural Development Under Irradiation in European ODS Ferritic/Martensitic Steels, *J. Nucl. Mater.*, 2006, **351**(1–3), p 247-260

19. C.H. Zhang, Y.T. Yang, Y. Song, J. Chen, L.Q. Zhang, J. Jang, and A. Kimura, Irradiation Response of ODS Ferritic Steels to High-Energy Ne ions at HIRFL, *J. Nucl. Mater.*, 2014, **455**(1–3), p 61-67

20. D.J. Barton, C. Kale, B.C. Hornbuckle, K.A. Darling, K.N. Solanki, and G.B. Thompson, Microstructure and Dynamic Strain Aging Behavior in Oxide Dispersion Strengthened 91Fe-8Ni-1Zr (at%) Alloy, *Mater. Sci. Eng. A*, 2018, **725**, p 503-509

21. P. Unifantowicz, Z. Oksiuta, P. Olier, Y. de Carlan, and N. Baluc, Microstructure and Mechanical Properties of an ODS RAF Steel Fabricated by Hot Extrusion or Hot Isostatic Pressing, *Fusion Eng. Des.*, 2011, **86**(9–11), p 2413-2416

22. K.A. Darling, M.A. Tschopp, R.K. Guduru, W.H. Yin, Q. Wei, and L.J. Kecskes, Microstructure and Mechanical Properties of Bulk Nanostructured Cu–Ta Alloys Consolidated by Equal Channel Angular Extrusion, *Acta Mater.*, 2014, **76**, p 168-185

23. L.N. Brewer, M.S. Bennett, B.W. Baker, E.A. Payzant, and L.M. Sochalski-Kolbus, Characterization of Residual Stress as a Function of Friction Stir Welding Parameters in Oxide Dispersion Strengthened (ODS) Steel MA956, *Mater. Sci. Eng. A*, 2015, **647**, p 313-321

24. B.W. Baker, E.S.K. Menon, T.R. McNelley, L.N. Brewer, B. El-Dasher, J.C. Farmer, S.G. Torres, M.W. Mahoney, and S. Sanderson, Processing-Microstructure Relationships in Friction Stir Welding of MA956 Oxide Dispersion Strengthened Steel, *Metall. Mater. Trans. E*, 2014, **1**(4), p 318-330

25. B.W. Baker, T.R. McNelley, and L.N. Brewer, Grain Size and Particle Dispersion Effects on the Tensile Behavior of Friction Stir Welded MA956 Oxide Dispersion Strengthened Steel from Low to Elevated Temperatures, *Mater. Sci. Eng. A*, 2014, **589**, p 217-227

26. B. Maier, M. Lenling, H. Yeom, G. Johnson, S. Maloy, and K. Sridharan, A Novel Approach for Manufacturing Oxide Dispersion Strengthened (ODS) Steel Cladding Tubes Using Cold Spray Technology, *Nucl. Eng. Technol.*, 2019, **51**, p 1069-1074

27. B. Marzbanrad, H. Jahed, and E. Toyserkani, On the Evolution of Substrate's Residual Stress During Cold Spray Process: A Parametric Study, *Mater. Des.*, 2018, **138**, p 90-102

28. V. Luzin, K. Spencer, and M.X. Zhang, Residual Stress and Thermo-Mechanical Properties of Cold Spray Metal Coatings, *Acta Mater.*, 2011, **59**(3), p 1259-1270

29. M. Saleh, V. Luzin, and K. Spencer, Analysis of the Residual Stress and Bonding Mechanism in the Cold Spray Technique Using Experimental and Numerical Methods, *Surf. Coat. Technol.*, 2014, **252**, p 15-28

30. T. Suhonen, T. Varis, S. Dosta, M. Torrell, and J.M. Guilemany, Residual Stress Development in Cold Sprayed Al, Cu and Ti Coatings, *Acta Mater.*, 2013, **61**(17), p 6329-6337

31. S. Rech, A. Trentin, S. Vezzù, J.-G. Legoux, E. Irissou, and M. Guagliano, Influence of Pre-Heated Al 6061 Substrate Temperature on the Residual Stresses of Multipass Al Coatings Deposited by Cold Spray, *J. Therm. Spray Technol.*, 2010, **20**(1–2), p 243-251

32. F. Tölle, A. Gumenyuk, A. Backhaus, S. Olschok, M. Rethmeier, and U. Reisgen, Welding Residual Stress Reduction by Scanning of a Defocused Beam, *J. Mater. Process. Technol.*, 2012, **212**(1), p 19-26

33. S. Ghosh, J. Choi, 3-Dimensional Transient Residual Stress Finite Element Analysis for Laser Aided Direct Metal Deposition Process, in International Congress on Applications of Lasers & Electro-Opticsed., Unlisted, Ed., Laser Institute of America, 2003, p 1–12

34. J.H. Yao, L.J. Yang, B. Li, Q.L. Zhang, and Z.H. Li, Depoisition Characteristics and Microstructure of a Ni60-Ni Composite Coating Produced by Supersonic Laser Deposition, *Lasers Eng.*, 2017, **36**, p 117-131

35. H. Kotan, K.A. Darling, M. Saber, R.O. Scattergood, and C.C. Koch, An In Situ Experimental Study of Grain Growth in a Nanocrystalline $Fe_{91}Ni_8Zr_1$ Alloy, *J. Mater. Sci.*, 2012, **48**(5), p 2251-2257

36. K.A. Darling, B.K. VanLeeuwen, J.E. Semones, C.C. Koch, R.O. Scattergood, L.J. Kecskes, and S.N. Mathaudhu, Stabilized Nanocrystalline Iron-Based Alloys: Guiding Efforts in Alloy Selection, *Mater. Sci. Eng. A*, 2011, **528**(13–14), p 4365-4371

37. W.A. Story, Processing-microstructure-property relations in high pressure cold spray deposition of AA2024 and AA7075, The University of Alabama, 2018

38. C.E. Murray, I.C. Noyan, Applied and Residual Stress Determination Using X-ray Diffraction, Practical Residual Stress Measurement Methods, 1 ed., G.S. Schaier, Ed., (Wiley, New York, 2013)

39. H. Kotan, K.A. Darling, M. Saber, C.C. Koch, and R.O. Scattergood, Effect of Zirconium on Grain Growth and Mechanical Properties of a Ball-Milled Nanocrystalline FeNi Alloy, *J. Alloy. Compd.*, 2013, **551**, p 621-629

40. E. Liverani, A.H.A. Lutey, A. Ascari, A. Fortunato, and L. Tomesani, A Complete Residual Stress Model for Laser Surface Hardening of Complex Medium Carbon Steel Components, *Surf. Coat. Technol.*, 2016, **302**, p 100-106

41. S. Mates, M. Stoudt, and S. Gangireddy, Measuring The Influence of Pearlite Dissolution on the Transient Dynamic Strength of Rapidly-Heated Plain Carbon Steels, *JOM (1989)*, 2016, **68**(7), p 1832-1838

42. S. Denis, P. Archambault, C. Aubry, A. Mey, J.C. Jouin, and A. Simon, Modelling Of Phase Transformation Kinetics in Steels and Coupling with Heat Treatment Residual Stress Predictions, *J. Phys. IV*, 1999, **9**(PR9), p 323-332

43. J. Sakkiettibutra and E.N. Kamau, Influence of Austenitisation and Transformation Hardening on the Residual Stress Development of Laser Beam Treated Components made of 20MnCr5, *Materialwiss. Werkstofftech.*, 2012, **43**(1–2), p 171-177

44. N.S. Bailey, W. Tan, and Y.C. Shin, Predictive Modeling and Experimental Results for Residual Stresses in Laser Hardening of AISI, 4140 Steel by a High Power Diode Laser, *Surf. Coat. Technol.*, 2009, **203**(14), p 2003-2012

45. W. Li, K. Yang, D. Zhang, and X. Zhou, Residual Stress Analysis of Cold-Sprayed Copper Coatings by Numerical Simulation, *J. Therm. Spray Technol.*, 2015, **25**(1–2), p 131-142

46. A.S. Franchim, V.S. Campos, D.N. Travessa, and C.M. Neto, Analytical Modelling for Residual Stresses Produced by Shot Peening, *Mater. Des.*, 2009, **30**(5), p 1556-1560

Publisher's Note Springer Nature remains neutral with regard to jurisdictional claims in published maps and institutional affiliations.